

ABSTRACT

Annular patterns with a high degree of zonal symmetry play a prominent role in the natural variability of the atmospheric circulation and its response to external forcing. But despite their apparent importance for understanding climate variability, the processes that give rise to their marked zonally symmetric components remain largely unclear.

Here the authors use simple stochastic models in conjunction with atmospheric model and observational analyses to explore the conditions under which annular patterns arise from Empirical Orthogonal Function (EOF) analysis of the flow. The results indicate that annular patterns arise not only from zonally coherent fluctuations in the circulation, i.e., “dynamical annularity”, but also from zonally symmetric statistics of the circulation in the absence of zonally coherent fluctuations, i.e., “statistical annularity”. It is argued that the distinction between dynamical and statistical annular patterns derived from EOF analysis can be inferred from the associated variance spectrum: larger differences in the variance explained by an annular EOF and successive EOFs generally indicate underlying dynamical annularity.

The authors provide a simple recipe for assessing the conditions that give rise to annular EOFs of the circulation. When applied to numerical models, the recipe indicates dynamical annularity in parameter regimes with strong feedbacks between the eddies and mean flow. When applied to observations, the recipe indicates that annular EOFs generally derive from statistical annularity of the flow in the middle latitude troposphere, but from dynamical annularity in both the stratosphere and the mid-high latitude Southern Hemisphere troposphere.

1. Introduction

“Annular” patterns of variability are structures dominated by their zonally symmetric components. They emerge as the leading empirical orthogonal functions (EOFs) of the Northern Hemisphere sea-level pressure field (Lorenz 1951; Kutzbach 1970; Wallace and Gutzler 1981; Trenberth and Paolino 1981; Thompson and Wallace 1998, 2000), the Southern Hemisphere zonal-wind and geopotential height fields (Kidson 1988; Karoly 1990; Hartmann and Lo 1998; Thompson and Wallace 2000; Lorenz and Hartmann 2001), the Southern Hemisphere eddy-kinetic field (Thompson and Woodworth 2014), the extratropical circulation in a hierarchy of numerical simulations of the atmospheric circulation (e.g., Robinson 1991; Yu and Hartmann 1993; Lee and Feldstein 1996; Shindell et al. 1999; Gerber and Vallis 2007), and aquaplanet simulations of the ocean circulation (Marshall et al. 2007). They are seemingly ubiquitous features in a range of geophysical flows.

Despite their ubiquity in the climate system, one key aspect of annular structures remains open to debate: What gives rise to their marked zonally symmetric components? Does the zonal symmetry of annular structures reflect coherent variations in climate across a range of longitudes? Or does it largely reflect the constraints of EOF analysis (e.g., Dommenges and Latif 2002; Gerber and Vallis 2005)? Consider a long-standing example: the so-called northern annular mode (NAM) emerges as the leading EOF of the NH sea-level pressure field (e.g., Thompson and Wallace 2000). It exhibits a high degree of zonal symmetry and its structure implies in-phase variability in climate between the North Atlantic and North Pacific sectors of the hemisphere. But as discussed extensively in earlier papers (e.g., Deser 2000; Ambaum et al. 2001), the two midlatitude centers of action of the NAM do not exhibit robust correlations on month-to-month timescales. Does the annularity of the NAM arise from dynamic connections between widely separated longitudes that are simply masked by other forms of variability (e.g., Wallace and Thompson 2002)? Or does the annularity arise from the constraints of the EOF analysis (e.g., Dommenges and Latif 2002; Gerber and Vallis 2005; Monahan et al. 2009)?

53 The purpose of this paper is to revisit the conditions that give rise to annular structures
54 in the leading patterns of variability of the circulation. We will demonstrate that annular
55 patterns can arise from two distinct characteristics of the flow: (i) “dynamical annularity”,
56 where variability in the circulation about its mean state exhibits in-phase correlations at all
57 longitudes, and (ii) “statistical annularity”, where the statistics of the flow (e.g., the variance,
58 autocorrelation and spatial decorrelation scale) are similar at all longitudes. Both conditions
59 can give rise to annular-like EOFs that make important contributions to the variability in
60 the circulation. But only the former corresponds to coherent annular motions in the flow.
61 Section 2 explores the impacts of “dynamical annularity” vs. “statistical annularity” on
62 EOF analysis of output from two simple stochastic models. Section 3 provides theoretical
63 context for interpreting the results of the simple models. Section 4 applies the insights
64 gained from the simple models to the circulation of an idealized general circulation model
65 and observations. Conclusions are provided in Section 5.

66 2. A Tale of Two Annular Modes

67 In the following, we define *dynamical annularity* as the case where there are positive
68 covariances between all longitudes around the globe, i.e.,

$$\text{cov}_X(\lambda_1, \lambda_2) = \frac{\sum_{n=1}^N X(\lambda_1, t_n)X(\lambda_2, t_n)}{N} > 0 \quad (1)$$

69 for all longitudes λ_1 and λ_2 . With this notation, we take X to be a generic variable of interest
70 (e.g., geopotential height or eddy kinetic energy), given as an anomaly from its climatological
71 mean. If (1) is satisfied, there are coherent underlying motions which cause the circulation
72 to vary in concert at all longitudes, and the integrated covariance around the latitude circle
73 provides a quantitative measure of the importance of the dynamical annularity.

74 We define *statistical annularity* as the case where the statistics of the flow do not vary

75 as a function of longitude, i.e.,

$$\text{cov}_X(\lambda_1, \lambda_2) = f(\Delta\lambda). \quad (2)$$

76 where $\Delta\lambda = |\lambda_1 - \lambda_2|$ is the absolute distance between the two points. This definition
77 implies that the variance of the flow is uniform, i.e. $f(0)$, and the covariance between any
78 two longitudes depends only on the distance between them, but not where the two points lie
79 relative to the origin (prime meridian). The criteria for dynamical and statistical annularity
80 are not mutually exclusive, and a flow could satisfy both at once. One would only expect
81 (2) to hold approximately in the presence of realistic boundary conditions, but in Section 4
82 we show the statistics of the observed atmosphere are remarkably annular, particularly in
83 the Southern Hemisphere.

84 Here we illustrate how statistical annularity can give rise to an annular EOF, even in
85 the case where there is no underlying dynamical annularity in the circulation (that is, the
86 motions are explicitly local). We consider two 1-dimensional stochastic models, $X_1(\lambda, j)$
87 and $X_2(\lambda, j)$. The details of the models are given in the Appendix, but all the necessary
88 statistics of the models are summarized in Fig. 1. In short, both models are random processes
89 in longitude, are periodic over 360° , and have zonally uniform statistics (2). The distinction
90 between the models lies in their covariance structures (Fig. 1c). For model X_1 , there is
91 explicitly no global correlation: variability at a given location is only correlated with other
92 longitudes over a range of about $\pm 90^\circ$. For model X_2 there is a global correlation of 0.1.

93 Note that since both models have zonally uniform statistics, the covariance structures
94 shown in Fig. 1c are independent of the base longitude used in the calculations. Moreover,
95 they contain all the information needed to characterize the EOFs of the two models; recall
96 that EOFs correspond to the eigenvectors of the covariance matrix $c_{ij} = \text{cov}_X(\lambda_i, \lambda_j)$. When
97 the statistics are uniform, c_{ij} is simply a function of the distance between λ_i and λ_j , as
98 illustrated in Fig. 1c.

99 The top three EOFs for the two models are shown in Fig. 2a and b. By construction (see
100 discussion in the next section), both models exhibit exactly the same EOFs. The first EOF

101 is perfectly annular, as the analytic formulation of the model allows us to take the limit of
102 infinite sampling. As seen in Fig. 2c, the first EOF also explains exactly the same fraction
103 of the variance in each model: 20%. The second and third EOFs characterize wavenumber 1
104 anomalies: all higher order EOFs come in sinusoidal pairs, increasing in wavenumber. The
105 phase is arbitrary, as the two wavenumber 1 modes explain the same fraction of variance. For
106 finite sampling, one would see slight mixing between the wavenumbers, but the top modes
107 are well established, even for a reasonable number of samples.

108 The key result in Fig. 2 is that both models exhibit a robust “annular mode” as their
109 leading EOF, and that both annular modes explain the same total fraction of the variance.
110 Only one of the apparent “annular modes”, however, reflects dynamical annularity in the
111 flow.

112 From the perspective of EOFs, one can only distinguish the two models by examining
113 their EOF spectra, i.e., the relative variance associated with all modes (Fig. 2c). By design,
114 the annular modes (the leading EOFs) in both models explain the same fraction of the total
115 variance (20%). The key differences between the EOF spectra from the two models lie in the
116 relative variance explained by their higher order EOFs. In the case of model 1, the first EOF
117 explains only slightly more variance than the second or third EOFs. In the case of model 2,
118 there is a large gap between the first and second EOFs. It is the relative variance explained
119 that provides insight into the relative importance of statistical vs. dynamical annularity in
120 giving rise to an annular-like leading EOF.

121 The stochastic models considered in Figs. 1 and 2 highlight two key aspects of annular
122 modes. First the models make clear that identical annular-like patterns can arise from two
123 very different configurations of the circulation: (i) cases where the statistics of the flow are
124 zonally uniform but the correlations are explicitly local (model 1) and (ii) cases with in-phase
125 variability between remote longitudes (model 2). Second, the models make clear that the
126 spectra of variance yields insight into the role of dynamical annularity in driving the leading
127 EOF.

3. Theoretical Insight

For systems with statistical annularity, as in models X_1 and X_2 , the EOFs can be entirely characterized based on the covariance structure $f(\Delta\lambda)$. Batchelor (1953) solved the EOF problem for cases with zonally uniform statistics in his analysis of homogeneous, isotropic turbulence in a triply periodic domain. Our discussion is the 1-D limit of this more comprehensive analysis. If the statistics are zonally uniform (i.e., homogeneous), then EOF analysis will yield a pure Fourier decomposition of the flow. All EOFs will come in degenerate pairs expressing the same fraction of variance, except for the single wavenumber 0 (annular) mode.

The ordering of the Fourier coefficients depends on the Fourier decomposition of f . The covariance function $f(\Delta\lambda)$ is defined for $0 \leq \Delta\lambda \leq \pi$, where we express longitude in radians. The variance associated with a mode of wavenumber k is then given by

$$\text{var}(k) = \frac{1}{\pi} \int_0^\pi f(\lambda) \cos(k\lambda) d\lambda \quad (3)$$

For all k other than 0, there will be two modes, each characterizing this amount of variance.

Setting $k = 0$ in (3) shows that the integral of the covariance function determines the variance associated with the annular mode. If we normalize the covariance function by $f(0)$ to obtain the correlation, the integral in turn provides the relative variance. For systems with zonally uniform statistics, there is thus a nice interpretation of the strength of the annular mode: the fraction of the variance expressed by the annular mode is simply the “average” of the correlation function between a given base point and all other points. This will hold even in cases where the annular mode is not the first EOF.

Returning to the simple stochastic models in Section 2, we can now see how the two models were designed to have the same annular mode. Given that the variance at each grid point was set to 1 by construction, the covariance functions are equivalent to the correlation functions. The average correlation in Fig. 1c is 0.2 in both cases, so that the “annular mode” in each model explains 20% of the total variance. In model X_1 , the average correlation of 0.2 derives solely from the strong positive correlation over half a hemisphere. That is, the

153 annular mode is the most important EOF, but it only reflects the annularity of the statistics.
 154 In model X_2 , half of the variance associated with the annular mode can be attributed to
 155 dynamical annularity, as given by the global baseline correlation of 0.1. The other half is
 156 attributable to the positive correlation on local scales, reflecting the spatial redness of the
 157 circulation.

158 Model X_2 shows that even in a system with dynamical annularity, the “strength” of the
 159 annular model is enhanced by the spatial redness of the flow, which exists independent of
 160 underlying dynamical annularity. The weaker spatial redness of the flow in model X_2 relative
 161 to X_1 is visibly apparent in the structure of its samples (compare Fig. 1a and b), while the
 162 presence of coherent dynamical annularity leads to the large gap between the fraction of
 163 variance associated with wavenumber 0 and other waves in the EOF spectrum in Fig. 1c.
 164 It follows that an annular EOF is more likely to reflect dynamical annularity when there is
 165 large separation between the variance explained by it and higher order modes. In this case,
 166 the average correlation over all longitudes arises from far field correlation and not simply
 167 the local positive correlations associated with the spatial redness of the circulation.

168 The models in Section 2 are two examples from a family of stochastic systems with spatial
 169 correlation structure

$$f(\lambda) = (1 - \beta)e^{-(\lambda/\alpha)^2} + \beta, \quad (4)$$

170 illustrated graphically in Fig. 3a. The parameter α is the spatial decorrelation scale (defined
 171 as the Gaussian width of the correlations in units of radians) and parameter β is the baseline
 172 annular correlation of the model. For systems with this spatial decorrelation structure, the
 173 leading EOF is always annular and the second and third EOFs always have wave 1 structure,
 174 even if there is no annular correlation (i.e., $\beta = 0$). This follows from the fact that a Fourier
 175 transform of a Gaussian is a Gaussian, such that power is always maximum at zero and
 176 decays with higher wavenumbers.

177 Fig. 3b summarize the variance explained by the leading EOFs of the system considered
 178 in Fig. 3a as a function of the spatial decorrelation scale (ordinate) and the amplitude of

179 the baseline annular correlation (abscissa). The contours indicate the variance explained
 180 by the leading (annular) EOF; the shading indicates the ratio of the variance between the
 181 leading and second (wavenumber one) EOFs. Dark blue shading indicates regions where
 182 the EOFs are degenerate (explain the same amount of variance). White shading indicates
 183 regions where the first EOF explains about twice the variance of the second EOF.

184 At the origin of the plot ($\alpha \rightarrow 0$ and $\beta = 0$), the system approaches the white noise limit,
 185 and all EOFs become degenerate. Traveling right along the x-axis from the origin (i.e.,
 186 keeping the spatial decorrelation scale α infinitesimally small and increasing the baseline
 187 annular correlation with β), we find that the variance associated with the wavenumber 0
 188 annular mode is simply given by the value of β . Here the spatial decorrelation scale collapses
 189 to a single longitude, so all higher modes are degenerate, and the strength of the annular
 190 mode derives entirely from dynamical annularity.

191 If one instead travels upward from the origin, allowing α to increase but keeping $\beta = 0$, the
 192 strength of the annular mode increases as well, despite their being no dynamical annularity.
 193 These are systems where the annular mode only reflects the *annularity of the statistics*, not
 194 *annularity of the motions*. As α gets increasingly large, positive correlations will develop
 195 at all longitudes by virtue of the fact that the spatial decorrelation scale is longer than a
 196 latitude circle. At this point, the spatial redness of the atmospheric motions gives rise to a
 197 baseline annular correlation due to the relatively short length of the latitude circle. When
 198 the spatial redness of the flow exceeds half of a latitude circle (0.5 on the ordinate axis),
 199 then the variance of the leading (annular) EOF explains \sim twice the variance of the second
 200 (wavenumber one) EOF.

201 Model 1 sits in the blue shaded region along the ordinate (see blue circle in Fig. 3b), with
 202 a spatial decorrelation scale of approximately 0.23 radians. Model 2 (the red square) was
 203 designed to have baseline annular correlation of 0.1 (i.e., $\beta = 0.1$), but with an annular mode
 204 that express the same fraction of variance, requiring a local correlation $\alpha \approx 0.13$ radians.

205 The simple models considered in this and the previous section provide insight into the

206 conditions that give rise to annular EOFs, and to the importance of the variance explained
207 by the leading EOFs in distinguishing between statistical and dynamical annularity. In the
208 following sections we apply these insights to output from a general circulation model and
209 observations. In the case of complex geophysical flows with out-of-phase correlations between
210 remote longitudes (i.e., teleconnections), one must consider not only the variance explained
211 by the leading EOFs, but also the spatial correlation structure $f(\Delta\lambda)$.

212 **4. The annularity of the circulation in models and re-** 213 **analysis**

214 How does the balance between dynamical vs. statistical annularity play out in general
215 circulation models and observations? In this section, we apply the insights gained from the
216 simple models to longitudinal variations of the atmospheric circulation at a single latitude,
217 e.g., variations in sea level pressure or geopotential height at 50°S. We focus on a single
218 latitude to provide a direct analogue to the simple one-dimensional stochastic models in
219 previous sections, albeit a single latitude serves as a stiff test for annular behavior. The
220 northern and southern annular mode patterns are based on EOF analysis of two-dimensional
221 SLP or geopotential height fields, where spherical geometry naturally connects the circulation
222 at all longitudes over the pole.

223 *a. Annular variability in a dry dynamical core*

224 We first consider a moisture free, 3-dimensional primitive equation model on the sphere,
225 often referred to as a dry dynamical core. The model is run with a flat, uniform lower
226 boundary, so that all the forcings are independent of longitude. Hence the circulation is
227 statistically annular, making it an ideal starting point to connect with the theory outlined
228 in the previous section.

229 The model is a spectral primitive equation model developed by the Geophysical Fluid Dy-
230 namics Laboratory (GFDL), run with triangular truncation 42 (T42) spectral resolution and
231 20 evenly spaced σ -levels in the vertical. It is forced with Held and Suarez (1994) “physics,”
232 a simple recipe for generating a realistic global circulation with minimal parameterization.
233 Briefly, all diabatic processes are replaced by Newtonian relaxation of the temperature to-
234 ward an analytic profile approximating an atmosphere in radiative-convective equilibrium,
235 and interaction with the surface is approximated by Rayleigh friction in the lower atmo-
236 sphere. The equilibrium temperature profile is independent of longitude and time, so there
237 is no annual cycle.

238 A key parameter setting the structure of the equilibrium temperature profile is the tem-
239 perature difference between the equator and pole, denoted $(\Delta T)_y$ by Held and Suarez (1994).
240 As explored in a number of studies (e.g., Gerber and Vallis 2007; Simpson et al. 2010;
241 Garfinkel et al. 2013), the strength of coupling between the zonal mean jet and baroclinic
242 eddies is sensitive to the meridional structure of the equilibrium temperature profile. A
243 weaker temperature gradient leads to stronger zonal coherence of the circulation and en-
244 hanced persistence of the annular mode. We use this sensitivity to contrast integrations
245 with varying degrees of dynamical annularity.

246 The temperature difference $(\Delta T)_y$ strongly influences the climatology of the model, as
247 illustrated by the near surface winds (blue curves) in Fig. 4, and can be compared with
248 similar results based on ERA-Interim reanalysis in Fig. 6. The results are based on 10,000
249 day integrations, exclusive of a 500 day spin up. The default setting for $(\Delta T)_y$ is 60° C, and
250 drives a fairly realistic equinoctial climatology with jets at 46° latitude in both hemispheres.
251 With a weaker temperature gradient, $(\Delta T)_y = 40^\circ$ C, the jets weaken and shifts equatorward
252 to approximately 38° .

253 The annular modes – defined as the first EOFs of daily zonal mean SLP – are illustrated
254 by the red curves in in Fig. 4 (the output is normalized by the square root cosine of latitude
255 before computing the EOFs, following Gerber et al. 2008; Baldwin and Thompson 2009).

256 By definition, the positive phase of the annular mode is defined as low SLP over the polar
257 region and thus a poleward shift of the model jet. We use the leading EOFs of SLP to
258 define the annular modes since SLP captures the barotropic component of the flow and is
259 frequently used in previous studies of annular variability (e.g., Thompson and Wallace 2000).
260 In practice, analyses of the near surface zonal wind field (not shown) yield the same patterns
261 of variability: the first principal component time series associated with the leading EOFs
262 of zonal mean SLP and 850 hPa zonal wind are strongly correlated, $R^2 = 0.92$ and 0.88 for
263 $(\Delta T)_y = 40$ and 60° C, respectively. The centers of action of the annular modes in sea level
264 pressure vary between the two simulations, and are indicated by vertical black lines. In the
265 following, we focus our analyses on latitudes corresponding to the centers of action of the
266 annular modes, contrasting it with similar analysis at their nodes.

267 The top row in Fig. 5 compares the spatial decorrelation structure of sea level pressure
268 anomalies as a function of longitude at these three key latitudes. Results for the integration
269 with weak and standard HS temperature gradients are indicated by blue and red colors,
270 respectively. The bottom row shows the variances explained by the leading EOFs of SLP
271 calculated along the same latitude bands (i.e., the EOFs are calculated as a function of
272 longitude and time along the indicated latitude bands). We applied a 10 day low pass Lanczos
273 filter (Duchon 1979) to the data before our analysis to reduce the influence of synoptic
274 scale variability, but the results are qualitatively similar when based on daily or monthly
275 mean data. To further reduce the sampling uncertainty, the autocorrelation functions were
276 averaged over all longitudes and the EOF spectra were computed directly with equation
277 (3). This has the effect of imposing zonally symmetric statistics, which would be the case
278 with infinite sampling, and the results are virtually identical if we use the full fields for the
279 calculations.

280 We focus first on the equatorward center of action of the annular mode (left column).
281 Variations in sea level pressure in this region are tightly linked with shifts in the midlatitude
282 jet, as evidenced by the high correlation between zonal mean SLP at this single latitude and

283 the first principal component of zonal mean zonal wind: $R^2 = 0.95$ and 0.94 for $(\Delta T)_y = 40$
 284 and 60° C, respectively. The spatial decorrelation scale of SLP anomalies is approximately
 285 60° longitude in both integrations (Fig. 5a). The east-west structure of the correlations
 286 reflects the scale of synoptic disturbances and wave trains emanating in both directions.
 287 The similarities between the spatial decorrelation scales reflects the fact that the deformation
 288 radius is similar in both runs. The most striking difference between the two runs lies in their
 289 baseline annular correlations. In the case of $(\Delta T)_y = 40$ the east-west structure of the
 290 correlations rides on top of a zonally uniform correlation of approximately 0.3 . In the case
 291 of the model with $(\Delta T)_y = 60$, there is a weaker baseline correlation of approximately 0.1 .

292 The difference in the underlying annularity of the flow explains the differences in the
 293 variance spectra shown in Fig. 5d. In both model configurations, the leading EOFs are
 294 annular; higher order modes generally increase monotonically in wavenumber with the ex-
 295 ception of waves 5 and 6, which explain larger fractions of the variance than waves 3 and 4,
 296 consistent with the synoptic structure of the correlation functions. The distinction between
 297 the EOFs between the two model configurations lies in their variance spectra. In the case
 298 of $(\Delta T)_y = 40$, the annular mode explains more than four times the variance of the second
 299 EOF. In the case of $(\Delta T)_y = 60$, the annular mode explains about two times the variance
 300 of the second EOF.

301 The differences in the variance spectra for the two model configurations are consistent
 302 with the theoretical arguments outlined in the previous section. Both model configurations
 303 exhibit dynamical annularity, as evidenced by the fact the spatial correlations are > 0 at all
 304 longitudes. However, the dynamical annularity is much more pronounced for the $(\Delta T)_y = 40$
 305 configuration, consistent with the larger ratio in variance explained between the first and
 306 second EOFs. The $(\Delta T)_y = 60$ configuration is reminiscent of the simple stochastic model
 307 X_2 , where the leading EOF explains approximately 20% of the variance in the flow: half due
 308 to the dynamical annularity; half due to the spatial redness of the flow.

309 The annularity of flow is notably different along the node of the annular mode, which is

310 strongly linked with variations in the strength of the jet stream. Zonal mean sea level pressure
311 here is highly correlated with the second EOF of zonal mean zonal wind, which characterizes
312 fluctuations in the strength and width of the jet (e.g., Vallis et al. 2004): $R^2 = 0.88$ and
313 0.83 for $(\Delta T)_y = 40$ and 60° C, respectively. The leading EOFs of SLP along the nodes
314 of the annular modes are again annular, as is the case at the equatorward centers of action
315 (not shown). But along this latitude, there is no apparent baseline annular correlation in
316 either model configuration (Fig. 5b). Accordingly, the EOF variance spectra exhibit little
317 distinction between the variance explained by the first and second EOFs. The enhanced
318 dynamical annularity in the $(\Delta T)_y = 40$ case is thus associated chiefly with vacillations
319 of the jet stream’s position, not fluctuations in its strength, which would be reflected by
320 dynamical annularity in SLP at this latitude.

321 At the minimum of the annular mode pattern on the poleward flank of the jet stream,
322 Fig. 5c and f, the relatively small size of the latitude circle leads to a strong baseline annular
323 correlation and thus clear dominance of the annular mode in the variance spectra. The
324 spherical effect is more pronounced for the $(\Delta T)_y = 60$ case since the minimum in the
325 EOF pattern is located very close to the pole (Fig. 4). As the length of the latitude circle
326 approaches the scale of the deformation radius, a single synoptic scale disturbance connects
327 all longitudes, enforcing zonally uniform statistics. While the result appears trivial in this
328 light, this geometric effect may play a significant role in helping the annular mode rise above
329 other modes in two-dimensional EOF analysis. The flow is naturally zonally coherent near
330 the pole, and the tendency for anticorrelation between pressures at polar and middle latitudes
331 may play a role in generating annular-scale motions at lower latitudes (e.g., Ambaum et al.
332 2001; Gerber and Vallis 2005).

333 It’s important to note that the circulation is more realistic with the default Held and
334 Suarez (1994) setting of $(\Delta T)_y = 60$, where the flow exhibits relatively modest zonal coher-
335 ence at the midlatitude center of action (Fig. 5a). The stronger dynamical annularity in the
336 $(\Delta T)_y = 40$ configuration is due to the weak baroclinicity of the jet and the zonally uniform

337 boundary conditions. When zonal asymmetries are introduced to the model, the uniform
338 motions are much reduced, even with weak temperature forcing (Gerber and Vallis 2007).
339 Zonal asymmetries on Earth will thus likely both reduce the strength of globally coherent
340 motions in the sense of equation (1), and break the assumption of uniform statistics in the
341 sense of equation (2). We find, however, that both dynamical and statistical annularity are
342 highly relevant to flow in reanalysis, at least in the Southern Hemisphere.

343 *b. Annular variability in reanalysis*

344 The data used in this section are derived from the European Center for Medium Range
345 Weather Forecasting (ECMWF) Interim Reanalysis (ERA-I; Dee and coauthors 2011) over
346 the period 1979 to 2013. All results are based on anomalies, where the annual cycle is defined
347 as the long-term mean over the entire 35 year period. As done for the dynamical core, a 10
348 day low pass filter is applied to all data before computing correlations and performing the
349 EOF analyses. Note that qualitatively similar results are derived from daily and monthly-
350 mean data.

351 Fig. 6 shows the meridional structures of (i) the climatological zonal mean zonal wind at
352 850 hPa and (ii) the southern and northern annular modes. The annular mode time series
353 are defined as the standardized leading PCs of zonal mean 850 hPa geopotential height,
354 Z_{850} , between 20-90 degrees latitude. Since the time series are standardized, the regression
355 patterns shown in Fig. 6 reveal the characteristic amplitude of a one standard deviation
356 anomaly in the annular modes. While the long-term mean circulation differs considerably
357 between the two hemispheres, the annular modes are remarkably similar, although the NAM
358 is slightly weaker than the SAM, consistent with the weaker climatological jet. Gerber and
359 Vallis (2005) suggest that the meridional structure of the annular modes tend to be fairly
360 generic, constrained largely by the geometry of the sphere and the conservation of mass and
361 momentum.

362 The longitudinal correlation structures derived from the observations are not constrained

363 to be uniform with longitude, as is the case for the dry dynamical core. Nevertheless, they are
 364 very similar from one base meridian to the next, particularly in the Southern Hemisphere.
 365 For example, Fig. 7a shows four single point covariance maps based on Z_{850} at 50°S : the
 366 covariance between Z_{850} at base points 0° , 90°E , 180° , and 90°W with all other longitudes.
 367 We have shifted the four regression plots so that the base points overlie each other at the
 368 center of the plot. Aside from slight variations in amplitude, there is remarkable uniformity
 369 of the east-west correlation structure in the midlatitudes Southern Hemisphere circulation:
 370 nearly all of the curves collapse upon each other. The correlation structures are positively
 371 correlated over a range of approximately ± 60 degrees longitude and exhibit alternating
 372 negative and positive lobes beyond that point. There is little evidence of global correlation,
 373 as is the case with the default Held and Suarez (1994) model.

374 Fig. 7b extends the analysis in the top panel to include averages over all base meridians for
 375 geopotential data at all latitudes. The figure is constructed as follows: (i) at a given latitude,
 376 we calculate the zonal covariance structure for all possible base meridians, as opposed to just
 377 four in Fig. 7a, (ii) we then average the resulting covariance structures after shifting them
 378 to a common base meridian, (iii) we normalize the resulting “average covariance structure”
 379 by the variance to convert to correlation coefficients, and lastly (iv) we repeat the analysis
 380 for all latitudes. The resulting “average correlation structures” for 850 hPa geopotential
 381 height are indicated by the shading in Fig. 7b. The black curve denotes the zero contour;
 382 the gray curves denote a distance of ± 2500 km from the base longitude to provide a sense
 383 of the sphericity of the Earth. Normalizing the covariance functions by the variance allows
 384 us to compare the longitudinal structures in the tropics and the midlatitudes on the same
 385 figure; otherwise the increase in the variance of Z_{850} with latitude (illustrated in Fig. 7c)
 386 yields much larger amplitudes in the extratropics.

387 At middle latitudes, positive correlations extend over a distance of approximately 2500
 388 km outward from the base longitude. Towards the polar regions, the autocorrelations extend
 389 over much of the latitude circle due to the increasingly smaller size of the zonal ring. The

390 austral polar regions are exceptional, in that the correlations extend not only around the
391 circumference of the latitude circle, but also well beyond 2500 km as far equatorward as
392 60°S. Interestingly, tropical geopotential height is also correlated over long distances. The
393 significant positive correlations at tropical latitudes are robust at most individual longitudes
394 outside of the primary centers of action of ENSO (not shown). The in-phase behavior
395 in tropical geopotential height is consistent with the dynamic constraint of weak pressure
396 gradients at tropical latitudes (Charney 1963; Sobel et al. 2001) and will be investigated
397 further in future work. Note that the amplitude of variations in geopotential height are
398 more than an order of magnitude weaker in the tropics than midlatitudes, as illustrated in
399 Fig. 7c.

400 The results shown in Fig. 7 are based on 10 day low pass filtered data. As discussed in
401 Wettstein and Wallace (2010), large-scale structures in the atmospheric circulation are in-
402 creasingly prevalent at lower frequency timescales. Analogous calculations based on monthly
403 mean data (not shown) reveal a slight extension of the region of positive correlations at all
404 latitudes, but overall the results are qualitatively unchanged. Notably, the midlatitude cor-
405 relation structure is still dominated by alternating negative and positive anomalies beyond
406 2500 km, with little evidence of zonally coherent motions.

407 How does the average correlation structure shown in Fig. 7b project onto the EOFs of
408 the circulation? Fig. 8 characterizes the (top) “predicted” and (bottom) “actual” EOFs of
409 zonally-varying Z_{850} calculated separately for each latitude (e.g., results at 60° N indicate the
410 variance expressed by EOFs of Z_{850} sampled along the 60° N latitude circle). The “predicted”
411 EOFs are found assuming the statistics of Z_{850} are zonally uniform. In this case, the results
412 of the EOF analysis correspond to a Fourier decomposition of the flow (see discussion in
413 Section 3), and the variance captured by each wavenumber is determined by the average
414 correlation structure (Fig. 7b) applied to (3). Wavenumber 0 (i.e., annular mode) variability
415 emerges as the leading predicted EOF of the flow at virtually all latitudes, but explains a
416 much larger fraction of the variance of the flow in the tropics and polar regions than it does

417 in middle latitudes, where wavenumbers 0, 1, 2, and 3 are of nearly equal importance. The
418 weak amplitude of wavenumber 0 variability in middle latitudes is consistent with the lack
419 of zonally coherent motions in the average correlation structures shown in Fig. 7b.

420 The “actual” EOFs are computed directly from Z_{850} , and thus do not assume that the
421 statistics of the flow are zonally uniform. Red dots indicate when the EOF is dominated
422 by wavenumber 0 variability, orange dots by wave 1 variability, and so forth for higher
423 wavenumbers. (Note that for the predicted EOFs, all wavenumbers other than 0 include two
424 modes in quadrature that account for equal variance, whereas for the actual EOFs, the two
425 modes associated with each wavenumber are not constrained to explain the same fraction of
426 the variance.) Comparing the top and bottom panels, it is clear that the EOFs predicted
427 from the average correlation structure, assuming zonally-uniform statistics, provide useful
428 insight into the true EOFs of the flow. The meridional structures of the variance explained
429 by the leading predicted and actual EOFs are very similar: in the high latitudes and tropics,
430 the first mode is dominated by wavenumber 0 variability and explains a much larger fraction
431 of the flow than EOF2; in the midlatitudes, the EOFs cluster together and are largely
432 degenerate.

433 The key point derived from Figs. 7 and 8 is that the “average correlation function” pro-
434 vides a clear sense of where the EOFs of the flow derive from robust dynamical annularity.
435 The circulation exhibits globally coherent motions in the tropics and high latitudes, partic-
436 ularly in the SH high latitudes (Fig. 7), and it is over these regions that the leading EOFs
437 predicted from the average correlation function (Fig. 8a) and from actual variations in the
438 flow (Fig. 8b) exhibit robust wavenumber 0 variability. In contrast, the circulation does
439 not exhibit globally coherent variations at middle latitudes (Fig. 7b), and thus both the
440 predicted and actual EOFs of the flow are degenerate there (Fig. 8). *Annular variations in*
441 *lower tropospheric geopotential height are consistent with dynamical annularity of the flow*
442 *in the polar and tropical regions, but statistical annularity at middle latitudes.*

443 Fig. 9 explores the average correlation structure in three additional fields. Fig. 9a,b show

444 results based on the zonal wind at 850 hPa (U_{850}), which samples the barotropic component
 445 of the circulation, and thus emphasizes the eddy-driven jet in middle latitudes. Fig. 9c,d are
 446 based on the zonal wind at 50 hPa and (U_{50}), which samples both the QBO and variations in
 447 the stratospheric polar vortices, and Fig. 9e,f, the eddy kinetic energy at 300 hPa (EKE_{300}),
 448 which samples the baroclinic annular mode (Thompson and Barnes 2014).

449 The most pronounced zonal correlations in U_{850} are found in two locations: (i) along
 450 60 degrees South, where positive correlations wrap around the latitude circle, and (ii) in
 451 the deep tropics, where positive correlations extend well beyond the 2500 km isopleths. At
 452 ~ 60 degrees South, the zonally coherent variations in the zonal flow follow from geostrophic
 453 balance and the coherence of the geopotential height field over Antarctica, as observed in
 454 Fig. 7b. In the subtropics, the far reaching correlations follow from geostrophic balance
 455 and the coherence of the geopotential height field in the tropics. At the equator, where
 456 geostrophic balance does not hold, Z_{850} exhibits globally coherent motions (consistent with
 457 weak temperature gradients in the tropics), while U_{850} becomes significantly anticorrelated
 458 at a distance. As a result, a zonally uniform annular mode dominates the EOF spectrum
 459 of Z_{850} in the tropics (Fig. 8b) whereas wavenumber 1 tends to dominate latitudinal EOF
 460 analysis of U_{850} (not shown). Neither Z_{850} (Fig. 7b) or U_{850} (Fig. 9a) exhibit zonally coherent
 461 motions at midlatitudes, where the autocorrelation function decays to zero ~ 2500 kilometers
 462 and oscillates in the far field.

463 The results shown in Figs. 7b and 9a are representative of the correlation structure of
 464 geopotential height and zonal wind throughout the depth of the troposphere (e.g., very
 465 similar results are derived at 300 hPa; not shown). However, the correlation structure of the
 466 zonal flow changes notably above the tropopause, as indicated in Fig. 9c and d. Consistent
 467 with the increase in the deformation radius in the stratosphere, the scale of motions increases
 468 (note that the grey lines now indicate the $\pm 5,000$ km isopleths). The most notable differences
 469 between the troposphere and stratosphere are found in the tropics, where the Quasi Biennial
 470 Oscillation (QBO) leads to an overwhelming annular signal. Marked annularity is also found

471 in the high latitudes, in the vicinity of both extratropical polar vortices. As observed in the
472 analysis of the tropospheric zonal wind and geopotential height, however, there is no evidence
473 of dynamical annularity in the midlatitudes.

474 The average correlation structure of EKE_{300} (Fig. 9e) is notably different. Unlike Z or
475 U , the zonal correlation of EKE is remarkably similar across all latitudes, with a slight
476 peak in the physical scale of the correlation in the Southern Hemisphere midlatitudes where
477 the baroclinic annular mode has largest amplitude (e.g., Thompson and Woodworth 2014).
478 Interestingly, EKE_{300} remains positively correlated around the globe at all latitudes, albeit
479 very weakly in the far field. The non-negative decorrelation structure leads to the dominance
480 of a zonally uniform “annular mode” in EKE at each individual latitude poleward of 25°S,
481 as shown in Fig. 10. However, the separation between the first and second modes (which
482 characterize wavenumber 1 motions) is modest at most latitudes. The largest separations
483 between the first and second EOFs EKE_{300} are found near 45°, where the top annular EOF
484 represents about 16% of the variance, compared to about 11% for the second and third
485 EOFs.

486 *c. Quantifying the role of dynamical annularity in EKE_{300} with the stochastic model*

487 At first glance, the weak separation between the first and second EOFs of EKE_{300}
488 suggests that much of the annular signal owes itself to local correlations, i.e., statistical
489 annularity. However, a comparison of the EOFs of the observations with those derived
490 from the “Gaussian + baseline” model explored in Sections 2 and 3 allows us to be more
491 quantitative about the relative role of dynamical vs. statistical annularity in the context of
492 the baroclinic annular mode.

493 Fig. 11 compares (a) the zonal correlation structure and (b) EOF spectrum of the 300
494 hPa eddy kinetic energy at 46°S with three fits of the simple stochastic model, each designed
495 to capture key features of the observed behavior. Recall that the model has two parameters:
496 the width of local correlation, α , and the baseline correlation strength, β . As our goal is to

497 focus on the relative role of dynamical annularity, characterized by the difference between
 498 the variance expressed by the top EOF (annular mode) and higher order modes, we remove
 499 one degree of freedom by requiring that the top EOF express the same fraction of variance in
 500 both the simple model and the reanalysis. Hence the first mode explains 16% of the variance
 501 for all cases in Fig. 11b. From equation (3), this condition is equivalent to keeping the total
 502 integral of the correlation structure fixed.

503 In the first fit (red curve, Fig. 11a), we optimize the stochastic model at short range,
 504 approximating the fall in local correlation in EKE as a Gaussian with width $\alpha = 17$ degrees.
 505 To maintain the variance expressed by the top EOF, parameter β must then be set to 0.08.
 506 This choice effectively lumps the midrange shoulder of the EKE_{300} correlation (30-100°)
 507 with the long range (100-180°), where the observed correlation drops to about 0.03. As
 508 a result, the stochastic model exhibits a stronger separation between the first and second
 509 EOFs than for EKE_{300} (red triangles vs. black squares in Fig. 11b).

510 An advantage of fitting the data to the simple stochastic model is that it allows us to
 511 explicitly quantify the role of dynamical annularity. Since the variance expressed by the
 512 annular mode is just the integral of correlation function (equation 3), the contribution of the
 513 long range correlation (dynamical annularity) to the total power of the annular mode is:

$$\frac{\int_0^{180} \beta d\lambda}{\int_0^{180} [(1 - \beta)e^{-(\lambda/\alpha)^2} + \beta] d\lambda} \approx \frac{\beta}{\frac{\alpha(1-\beta)\sqrt{\pi}}{360} + \beta} \quad (5)$$

514 where we have expressed longitude λ and parameter α in degrees. For the approximation
 515 on the left hand side, we assume that $\alpha \ll 180$, such that the local correlation does not
 516 significantly wrap around the latitude circle. For the “red” model in Fig. 11, dynamical
 517 annularity accounts for half of the total strength of the annular mode. Given the fact that it
 518 exhibits a stronger separation between the first and second EOFs, however, this is an upper
 519 bound on the role of dynamical annularity in EKE_{300} at 46°S.

520 We obtain a lower bound on the dynamical annularity with the blue fit in Fig. 11a, where
 521 the correlation structure is explicitly matched at long range. To conserve the total integral,
 522 parameter α in this case must be set to 27°, effectively lumping in the shoulder between

523 30 and 100° with the local correlation. These parameters would suggest that dynamical
524 annularity contributes only 1/5th of annular mode variance. This is clearly a lower limit,
525 however, as the separation between the first and second EOFs (Fig. 11b) is too small relative
526 to that of EKE_{300} .

527 Lastly, we use both degrees of freedom of the stochastic model to find an optimal fit of
528 the EOF spectrum, matching the variance expressed by the top two EOFs (effectively the
529 top three, as higher order modes come in pairs). The fit, with parameters $\alpha = 23^\circ$ and
530 $\beta = 0.05$, is not shown in Fig. 11a (to avoid clutter), but the resulting EOF spectrum is
531 illustrated by the green triangles in Fig. 11b. With this configuration, dynamical annularity
532 contributes approximately 1/3rd of the annular mode, leaving the remaining two thirds to
533 statistical annularity associated with the local redness of the EKE. The EOF spectra of this
534 model diverges from EKE_{300} for higher order modes, such that we should take this as a
535 rough estimate of the true role of dynamical annularity in the Baroclinic Annular Mode.

536 The location of the three models (lower, optimal, and upper bounds), are marked by the
537 black x's in Fig. 3b, to put them in context of earlier results. The fits roughly fill in the
538 space between models X_1 and X_2 , but on a lower contour where the annular mode expresses
539 16% of the total variance, as opposed to 20%. The rapid increase in the role of dynamical
540 annularity (from 1/5 to 1/2) matches the rapid ascent in the importance of EOF 1 relative
541 to EOF 2, emphasizing the utility of this ratio as an indicator of dynamical annularity.

542 5. Concluding Remarks

543 We have explored the conditions that give rise to annular patterns in Empirical Orthog-
544 onal Function analysis across a hierarchy of systems: highly simplified stochastic models,
545 idealized atmospheric GCMs, and reanalyses of the atmosphere. Annular EOFs can arise
546 from two conditions, which we term *dynamical annularity* and *statistical annularity*. The
547 former arises from zonally coherent dynamical motions across all longitudes, while the latter

548 arises from zonally coherent statistics of the flow (e.g., the variance), even in the absence of
549 significant far field correlations. Atmospheric reanalyses indicate that both play important
550 roles in the climate system and may aid in the interpretation of climate variability, but only
551 dynamical annularity reflects zonally coherent motions in the circulation.

552 In general, dynamical annularity arises when the dynamical scales of motion approach
553 the scale of the latitude circle. The average zonal correlation structure (e.g., Fig. 7) thus
554 provides a robust measure of dynamical annularity. In addition, the simple stochastic model
555 suggests that the degree of dynamical annularity in a leading EOF is indicated by the ratio
556 of the variances explained by the first two zonal EOFs of the flow. As a rule of thumb, if
557 the leading annular EOF explains more than twice the variance of the second EOF, then
558 dynamical annularity plays a substantial role in the annular mode. Note, however, that this
559 intuition does not necessarily apply to two-dimensional EOFs in latitude-longitude space,
560 where coherence of meridional variability can lead to dominance of an annular EOF, even
561 when there is explicitly no dynamical annularity (e.g., Gerber and Vallis 2005).

562 Annular EOFs always – at least partially – reflect statistical annularity of the circulation;
563 zonally coherent motions necessarily imply some degree of zonal coherence. Far field correla-
564 tion in the average zonal correlation structure robustly indicates dynamical annularity, but
565 quantification of the statistical annularity requires further analysis, either comparison of the
566 zonal correlation at different base points (e.g., Fig. 7a) or comparison of the predicted and
567 observed zonal EOFs (e.g., Figs. 8 and 10). The localization of the North Pacific and North
568 Atlantic storm tracks limits the utility of the zonal correlation structure in the Northern
569 Hemisphere troposphere. But the Southern Hemisphere tropospheric circulation is remark-
570 ably statistically annular, such that one can predict the full EOF spectrum from the average
571 correlation structure alone.

572 As discussed in Deser (2000) and Ambaum et al. (2001) and shown here, the observed
573 geopotential height and zonal wind fields do not exhibit robust far field correlations beyond
574 $\sim 60^\circ$ longitude in the midlatitudes (i.e., equatorward of roughly 60° latitude). However, the

575 geometry of the sphere naturally favors a high degree of zonal coherence at polar latitudes
576 in both hemispheres, particularly in the geopotential height field. Hence, the northern
577 and southern annular modes do not arise from dynamical annularity in the midlatitude
578 tropospheric circulation, but derive a measure of dynamical annularity from the coherence
579 of geopotential height within their polar centers of action. The dynamical annularity of
580 the polar geopotential height field extends to the zonal wind field at high latitudes ($\sim 60^\circ$
581 latitude) in the Southern Hemisphere, but less so in the Northern Hemisphere. Regions
582 where dynamical annularity plays a seemingly important role in the circulation thus include:

- 583 i. the geopotential height over polar latitudes in both hemispheres, which arises chiefly
584 from the geometry of the sphere,
- 585 ii. the zonal wind field near 60° latitude in the Southern Hemisphere, which exhibits
586 greater dynamical annularity than would be expected from the geometry of the sphere,
- 587 iii. the tropical geopotential height field, presumably because temperature gradients must
588 be weak in this region (e.g., Charney 1963),
- 589 iv. the tropospheric zonal flow near ~ 15 degrees latitude; these features arises via geostro-
590 phy and the dynamic annularity of the tropical Z field,
- 591 v. the zonal wind field in the equatorial stratosphere, which reflects the QBO,
- 592 vi. the eddy kinetic energy in the midlatitude Southern Hemisphere, consistent with the
593 baroclinic annular mode and the downstream development of wave packets in the
594 austral stormtrack (Thompson et al. submitted). The dynamical annularity of the
595 eddy activity is surprising given the lack of dynamic annularity in the midlatitude
596 barotropic jets, which are intimately connected with the eddies through the baroclinic
597 lifecycle.

598 The annular leading EOFs of the midlatitude flow have been examined extensively in

599 previous work, but to our knowledge, the annular nature of tropical tropospheric Z has
600 received less attention. We intend to investigate this feature in more detail in a future study.

601 *Acknowledgments.*

602 We thank two anonymous reviewers for constructive feedback on an earlier version of
603 this manuscript. EPG was supported by the National Science Foundation (NSF) through
604 grant AGS-1546585 and DWJT was supported by the NSF through the Climate Dynamics
605 Program.

606

607

Technical details of the stochastic models

608

609 The stochastic models in Section 2 are, in a sense, constructed in reverse, starting with
 610 the desired result. We begin with the correlation structure f , as shown in Fig. 1c, and
 611 project it onto cosine modes as in (3). This gives us the EOF spectra shown in Fig. 2c,
 612 i.e., how much variance (which we now denote v_k) should be associated with each mode of
 613 wavenumber k . Note that not all correlation structures are possible. A sufficient criteria,
 614 however, is that the projection of every cosine mode onto f is non-negative (i.e., all $v_k \geq 0$).

615 Realizations of the models, as shown in 1a and b, are constructed by moving back into
 616 grid space,

$$X(\lambda, j) = v_0^{1/2} \delta_{0,j} + \sum_{k=1}^{\infty} (2v_k)^{1/2} [\delta_{k1,j} \sin(k\lambda) + \delta_{k2,j} \cos(k\lambda)]. \quad (\text{A1})$$

617 where all the $\delta_{k,j}$ are independent samples from a Normal distribution with unit variance
 618 and λ is given in radians. In practise only the top 15 wavenumbers are needed, as the
 619 contribution of higher order modes becomes negligible.

620 Note that it is possible to construct an infinite number of stochastic systems which
 621 have the same correlation structure f . We have take a simple approach by using the Normal
 622 distribution to introduce randomness. Any distribution with mean zero could be used, which
 623 would impact the variations in individual samples – and so the convergence of the system in
 624 j – but not the statistical properties in the limit of infinite sampling.

REFERENCES

- 627 Ambaum, M. H. P., B. J. Hoskins, and D. B. Stephenson, 2001: Arctic Oscillation or North
628 Atlantic Oscillation? *J. Climate*, **14**, 3495–3507.
- 629 Baldwin, M. P. and D. W. J. Thompson, 2009: A critical comparison of stratosphere-
630 troposphere coupling indices. *Quart. J. Roy. Meteor. Soc.*, **135**, 1661–1672.
- 631 Batchelor, G. K., 1953: *The Theory of Homogeneous Turbulence*. Cambridge University
632 Press, 197 pp.
- 633 Charney, J. G., 1963: A note on large-scale motions in the tropics. *J. Atmos. Sci.*, **20**,
634 607–609.
- 635 Dee, D. P. and . coauthors, 2011: The ERA-Interim reanalysis: configuration and per-
636 formance of the data assimilation system. *Quart. J. Roy. Meteor. Soc.*, **137**, 553–597,
637 doi:10.1002/qj.828.
- 638 Deser, C., 2000: On the teleconnectivity of the "arctic oscillation". *Geophysical Research*
639 *Letters*, **27 (6)**, 779–782, doi:10.1029/1999GL010945.
- 640 Dommenges, D. and M. Latif, 2002: A cautionary note on the interpretation of EOFs. *J.*
641 *Climate*, **15**, 216–225.
- 642 Duchon, C. E., 1979: Lanczos filtering in one and two dimensions. *J. Applied Meteor.*, **18**,
643 1016–1022.
- 644 Garfinkel, C. I., D. W. Waugh, and E. P. Gerber, 2013: The effect of tropospheric jet latitude
645 on coupling between the stratospheric polar vortex and the troposphere. *J. Climate*, **26**,
646 2077–2095, doi:10.1175/JCLI-D-12-00301.1.

- 647 Gerber, E. P. and G. K. Vallis, 2005: A stochastic model for the spatial structure of annular
648 patterns of variability and the NAO. *J. Climate*, **18**, 2102–2118.
- 649 Gerber, E. P. and G. K. Vallis, 2007: Eddy-zonal flow interactions and the persistence of
650 the zonal index. *J. Atmos. Sci.*, **64**, 3296–3311.
- 651 Gerber, E. P., S. Voronin, and L. M. Polvani, 2008: Testing the annular mode autocorrelation
652 timescale in simple atmospheric general circulation models. *Mon. Wea. Rev.*, **136**, 1523–
653 1536.
- 654 Hartmann, D. L. and F. Lo, 1998: Wave-driven zonal flow vacillation in the Southern Hemi-
655 sphere. *J. Atmos. Sci.*, **55**, 1303–1315.
- 656 Held, I. M. and M. J. Suarez, 1994: A proposal for the intercomparison of the dynamical
657 cores of atmospheric general circulation models. *Bull. Am. Meteor. Soc.*, **75**, 1825–1830.
- 658 Karoly, D. J., 1990: The role of transient eddies in low-frequency zonal variations of the
659 southern hemisphere circulation. *Tellus A*, **42**, 41–50, doi:10.1034/j.1600-0870.1990.00005.
660 x.
- 661 Kidson, J. W., 1988: Interannual variations in the Southern Hemisphere circulation. *J.*
662 *Climate*, **1**, 1177–1198.
- 663 Kutzbach, J. E., 1970: Large-scale features of monthly mean Northern Hemisphere anomaly
664 maps of sea-level pressure. *Mon. Wea. Rev.*, **98**, 708–716.
- 665 Lee, S. and S. B. Feldstein, 1996: Mechanism of zonal index evolution in a two-layer model.
666 *J. Atmos. Sci.*, **53**, 2232–2246.
- 667 Lorenz, D. J. and D. L. Hartmann, 2001: Eddy-zonal flow feedback in the Southern Hemi-
668 sphere. *J. Atmos. Sci.*, **58**, 3312–3327.
- 669 Lorenz, E. N., 1951: Seasonal and irregular variations of the Northern Hemisphere sea-level
670 pressure profile. *J. Meteor.*, **8**, 52–59.

- 671 Marshall, J., D. Ferreira, J.-M. Campin, and D. Enderton, 2007: Mean climate and vari-
672 ability of the atmosphere and ocean on an aquaplanet. *J. Atmos. Sci.*, **64**, 4270–4286,
673 doi:10.1175/2007JAS2226.1.
- 674 Monahan, A. H., J. C. Fyfe, M. H. P. Ambaum, D. B. Stephenson, and G. R. North, 2009:
675 Empirical Orthogonal Functions: The Medium is the Message. *J. Climate*, **22**, 6501–6514,
676 doi:10.1175/2009JCLI3062.1.
- 677 Robinson, W. A., 1991: The dynamics of low-frequency variability in a simple model of the
678 global atmosphere. *J. Atmos. Sci.*, **48**, 429–441.
- 679 Shindell, D. T., R. L. Miller, G. A. Schmidt, and L. Pandolfo, 1999: Simulation of recent
680 northern winter climate trends by greenhouse-gas forcing. *Nature*, **399**, 452–455.
- 681 Simpson, I. R., M. Blackburn, J. D. Haigh, and S. N. Sparrow, 2010: The impact of the
682 state of the troposphere on the response to stratospheric heating in a simplified GCM. *J.*
683 *Climate*, **23**, 6166–6185.
- 684 Sobel, A. H., J. Nilsson, and L. M. Polvani, 2001: The weak temperature gradient approxi-
685 mation and balanced tropical moisture waves. *J. Atmos. Sci.*, **58**, 3650–3665.
- 686 Thompson, D. W. J. and E. A. Barnes, 2014: Periodic variability in the large-scale Southern
687 Hemisphere atmospheric circulation. *Science*, **343**, 641–645, doi:10.1126/science.1247660.
- 688 Thompson, D. W. J., B. R. Crow, and E. A. Barnes, submitted: Intraseasonal periodicity
689 in the southern hemisphere circulation on regional spatial scales. *J. Atmos. Sci.*
- 690 Thompson, D. W. J. and J. M. Wallace, 1998: The Arctic Oscillation signature in the
691 wintertime geopotential height and temperature fields. *Geophys. Res. Lett.*, **25**, 1297–
692 1300.
- 693 Thompson, D. W. J. and J. M. Wallace, 2000: Annular modes in the extratropical circulation.
694 Part I: Month-to-month variability. *J. Climate*, **13**, 1000–1016.

695 Thompson, D. W. J. and J. D. Woodworth, 2014: Barotropic and baroclinic annular
696 variability in the Southern Hemisphere. *J. Atmos. Sci.*, **71**, 1480–1493, doi:10.1175/
697 JAS-D-13-0185.1.

698 Trenberth, K. E. and D. A. Paolino, 1981: Characteristic patterns of variability of sea level
699 pressure in the Northern Hemisphere. *Mon. Wea. Rev.*, **109**, 1169–1189.

700 Vallis, G. K., E. P. Gerber, P. J. Kushner and B. A. Cash, 2004: A Mechanism and Simple
701 Dynamical Model of the North Atlantic Oscillation and Annular Modes. *J. Atmos. Sci.*,
702 **61**, 264–280.

703 Wallace, J. M. and D. S. Gutzler, 1981: Teleconnections in the geopotential height field
704 during the Northern Hemisphere winter. *Mon. Wea. Rev.*, **109**, 784–812.

705 Wallace, J. M. and D. W. J. Thompson, 2002: The Pacific center of action of the Northern
706 Hemisphere annular mode: Real or artifact? *J. Climate*, **15**, 1987–1991.

707 Wettstein, J. J. and J. M. Wallace, 2010: Observed patterns of month-to-month storm-track
708 variability and their relationship to the background flow. *J. Atmos. Sci.*, **67**, 1420–1437,
709 doi:10.1175/2009JAS3194.1.

710 Yu, J. Y. and D. L. Hartmann, 1993: Zonal flow vacillation and eddy forcing in a simple
711 GCM of the atmosphere. *J. Atmos. Sci.*, **50**, 3244–3259.

712 List of Figures

- 713 1 Two stochastic models of variability in longitude. (a) and (b) illustrate sample
714 profiles from models X_1 and X_2 , respectively. The profiles are independently
715 and identically sampled from the respective distribution of each model, but
716 could be interpreted as different realizations in time, chose over an interval
717 sufficiently large for the flow to lose all memory from one sample to the next.
718 The y-axes are unitless, as each model has been designed to have unit variance.
719 (c) shows $\text{cov}_X(0, \lambda)$ for each model, the covariance between variability at each
720 longitude with that at $\lambda = 0$. As the statistics are annular, the covariance
721 structure can be fully characterized by this one sample, i.e., $\text{cov}_X(\lambda_1, \lambda_2) =$
722 $\text{cov}_X(0, |\lambda_1 - \lambda_2|)$. 34
- 723 2 The EOF structure of the two stochastic models. (a) and (b) show the top
724 three EOFs for models 1 and 2, respectively, normalized to have unit variance.
725 In the limit of infinite sampling, the EOF patterns from the two models are
726 identical. (c) The models' EOF spectra, marking the fraction of the total
727 variance associated with each of the top 20 EOFs. 35
- 728 3 The impact of local vs. annular correlation in the “Gaussian + baseline”
729 family of stochastic models. (a) illustrates the parameters α and β which
730 characterize the correlation function $f(\lambda)$ for each model. (b) maps out the
731 variance expressed by the first EOF (black contours) and the ratio of the
732 variance expressed by the first EOF to that of the second (color shading) as a
733 function of α and β . The first EOF is always annular, and the second always a
734 wavenumber 1 pattern. The blue and red markers show the location of models
735 X_1 and X_2 (illustrated in Figs. 1 and 2) in parameter space, respectively; both
736 fall along the same black contour, as their top EOF expresses 0.2 of the total
737 variance. The black x's will be discussed in the context of Fig. 11 36

- 738 4 The mean jet structure and annular modes of the Held and Suarez (1994)
739 model for the (a) $(\Delta T)_y = 40$ and (b) $(\Delta T)_y = 60^\circ\text{C}$ integrations. The jet is
740 characterized by the time mean 850 hPa winds (blue lines, corresponding with
741 the left y-axes), and the annular mode is the first EOF of daily, zonal mean
742 SLP (red, right y-axes), normalized to indicate the strength of 1 standard
743 deviation anomalies. The latitudes of the node, equatorward and poleward
744 lobes of the annular mode are highlighted, and correspond with the analysis
745 in Fig. 5. 37
- 746 5 Characterizing the zonal structure of 10 day pass filtered SLP anomalies in
747 the Held and Suarez (1994) model. (a,d) and (c,f) show analysis based at
748 the latitude of the equatorward and poleward centers of action of the annular
749 mode, respectively, while (b,e) show analysis based at the nodes of the annular
750 mode. (a,b,c) show the zonal correlation structure $f(\lambda)$ and (d,e,f) the fraction
751 of variance associated with each of the top 20 EOFs for the integrations with
752 (blue) $(\Delta T)_y = 40$ and (red) $(\Delta T)_y = 60^\circ\text{C}$. 38
- 753 6 The same as Fig. 4, but for the (a) Southern and (b) Northern Hemispheres
754 in ECWMF Interim reanalysis, based on the period 1979-2013. To avoid
755 interpolation over mountainous regions, the annular modes are defined in
756 terms of daily, zonal mean 850 hPa geopotential height, Z_{850} , instead of SLP. 39

757 7 Characterizing the longitudinal correlation structure of 10 day low pass filtered
758 850 hPa geopotential height in ERA-Interim. (a) Sample single point corre-
759 lation maps at 46°S (the equatorward center of action of the SAM), shifted
760 so that base points line up. The black line is the mean of the four curves,
761 an “average single point correlation map”. (b) The average zonal correlation
762 structure of 10 day low pass filtered Z_{850} as a function of latitude. The con-
763 tour interval is 0.05, with black contours marking zero correlation, and gray
764 lines indicate a separation of 5000 km, to provide a sense of geometry on the
765 sphere. (c) The root mean square amplitude of 10 day low pass filtered Z_{850}
766 anomalies. 40

767 8 A comparison of predictions based on zonally uniform statistics to the actual
768 zonal EOF structure of 10 day low pass filtered Z_{850} . (a) For each latitude,
769 the fraction of variance associated with wavenumbers 0 to 6, given the average
770 zonal correlation structure in Fig. 7b and assuming zonally uniform statistics
771 (see text for details). (b) Again for each latitude, the fraction of variance
772 associated with the top five 1-D longitudinal EOFs, but now based on the full
773 flow. Large (small) colored dots indicate when a given wavenumber dominates
774 more than 75% (50%) of the power in the EOF, the color identifying the
775 respective wavenumber with the color convention in (a), i.e., red=wave 0,
776 orange=wave 1. 41

777 9 The average correlation structure of (a) zonal wind at 850 hPa, (c) zonal wind
778 at 50 hPa, and (e) eddy kinetic energy at 300 hPa. As in Fig. 7b, thin black
779 contours mark zero correlation and the thick gray contours give a sense of
780 sphericity, marking a separation of 5000 km as a function of latitude in (a)
781 and (e) and a distance of 10000 km in (c). Panels (b), (d), and (f) show
782 the root mean square amplitude of variations as a function latitude for each
783 variable, respectively. 42

- 784 10 The same as in Fig. 8b, but for eddy kinetic energy at 300 hPa. Zonal asym-
785 metry in the statistics lead to substantial mixing between wavenumbers in
786 the Northern Hemisphere (outside the polar cap) and tropics, such no sin-
787 gle wavenumber dominates each EOF. Statistical annularity in the Southern
788 Hemisphere, however, leads to a clearly order spectrum poleward of 25°S,
789 dominated by an annular (wavenumber 1) mode at all latitudes. 43
- 790 11 (a) Comparison between the average longitudinal correlation structure of
791 EKE_{300} at 46°S and two possible fits with the Gaussian + baseline model
792 of Section 3. As detailed in the text, the first fit (red) is optimized to cap-
793 ture the initial decay in correlation, while the second fit (blue) is optimized
794 for the long range correlation baseline. (b) The 1-dimensional EOF spectra
795 of EKE_{300} at 46°S, compared against the spectrum for the two fits of the
796 Gaussian + baseline model shown in (a), and a third model with parameters
797 $\alpha = 23^\circ$ and $\beta = 0.05$, as discussed in the text. 44

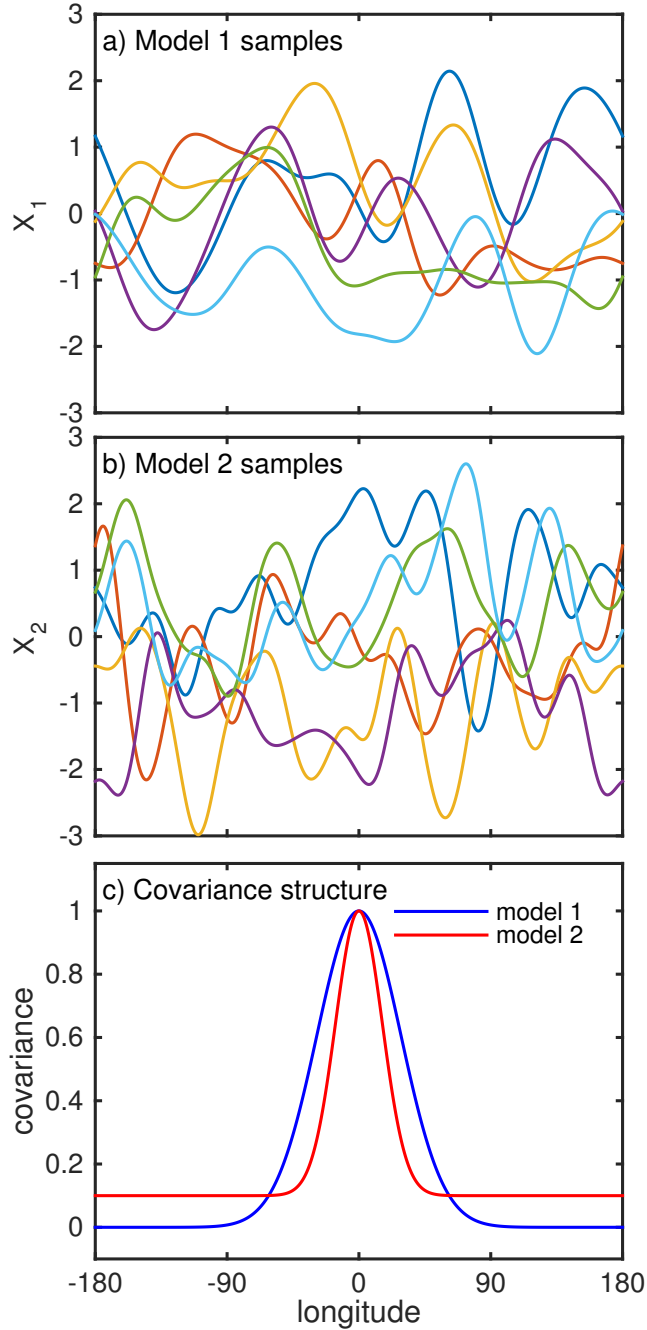


FIG. 1. Two stochastic models of variability in longitude. (a) and (b) illustrate sample profiles from models X_1 and X_2 , respectively. The profiles are independently and identically sampled from the respective distribution of each model, but could be interpreted as different realizations in time, chose over an interval sufficiently large for the flow to lose all memory from one sample to the next. The y-axes are unitless, as each model has been designed to have unit variance. (c) shows $\text{cov}_X(0, \lambda)$ for each model, the covariance between variability at each longitude with that at $\lambda = 0$. As the statistics are annular, the covariance structure can be fully characterized by this one sample, i.e., $\text{cov}_X(\lambda_1, \lambda_2) = \text{cov}_X(0, |\lambda_1 - \lambda_2|)$.

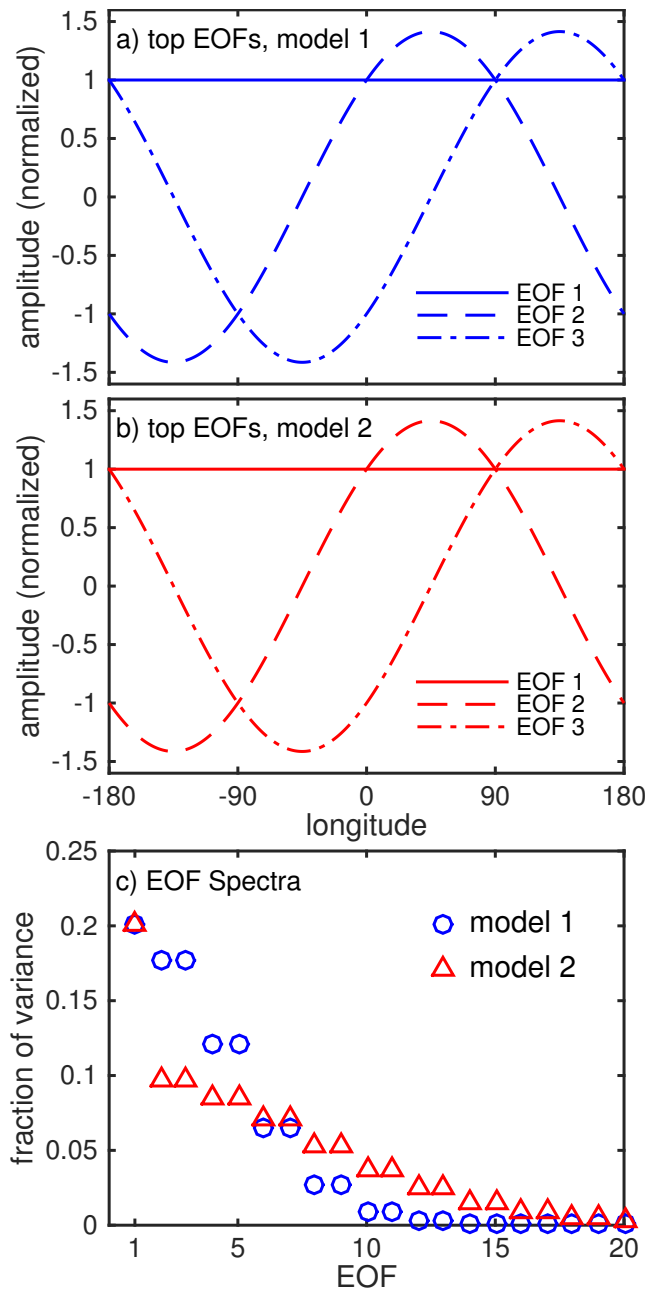


FIG. 2. The EOF structure of the two stochastic models. (a) and (b) show the top three EOFs for models 1 and 2, respectively, normalized to have unit variance. In the limit of infinite sampling, the EOF patterns from the two models are identical. (c) The models' EOF spectra, marking the fraction of the total variance associated with each of the top 20 EOFs.

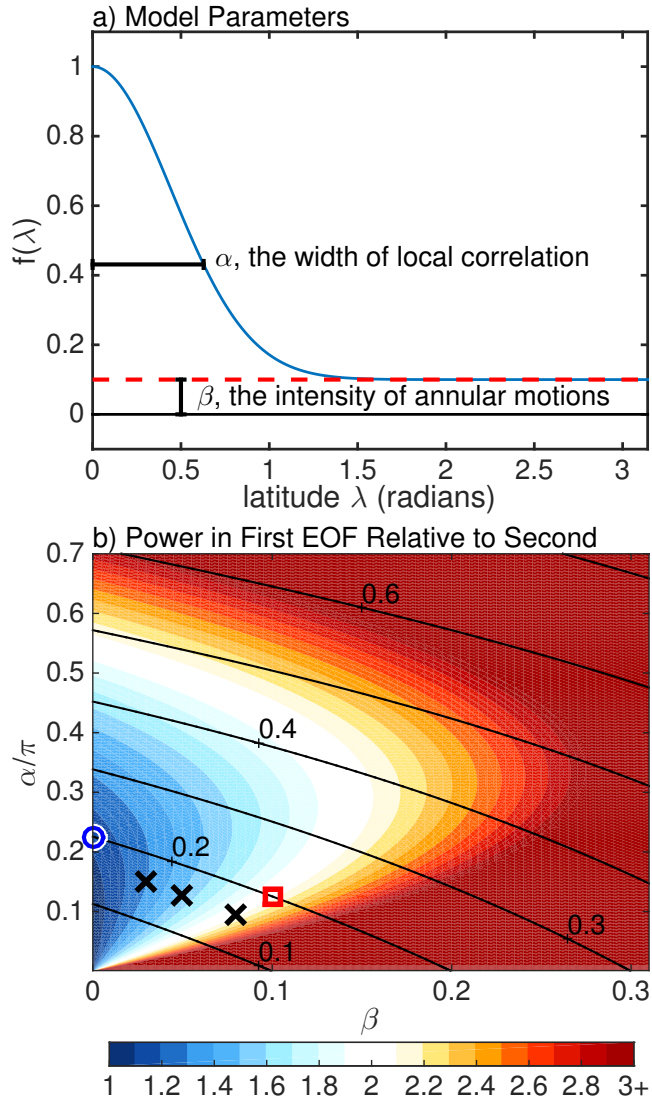


FIG. 3. The impact of local vs. annular correlation in the “Gaussian + baseline” family of stochastic models. (a) illustrates the parameters α and β which characterize the correlation function $f(\lambda)$ for each model. (b) maps out the variance expressed by the first EOF (black contours) and the ratio of the variance expressed by the first EOF to that of the second (color shading) as a function of α and β . The first EOF is always annular, and the second always a wavenumber 1 pattern. The blue and red markers show the location of models X_1 and X_2 (illustrated in Figs. 1 and 2) in parameter space, respectively; both fall along the same black contour, as their top EOF expresses 0.2 of the total variance. The black x’s will be discussed in the context of Fig. 11

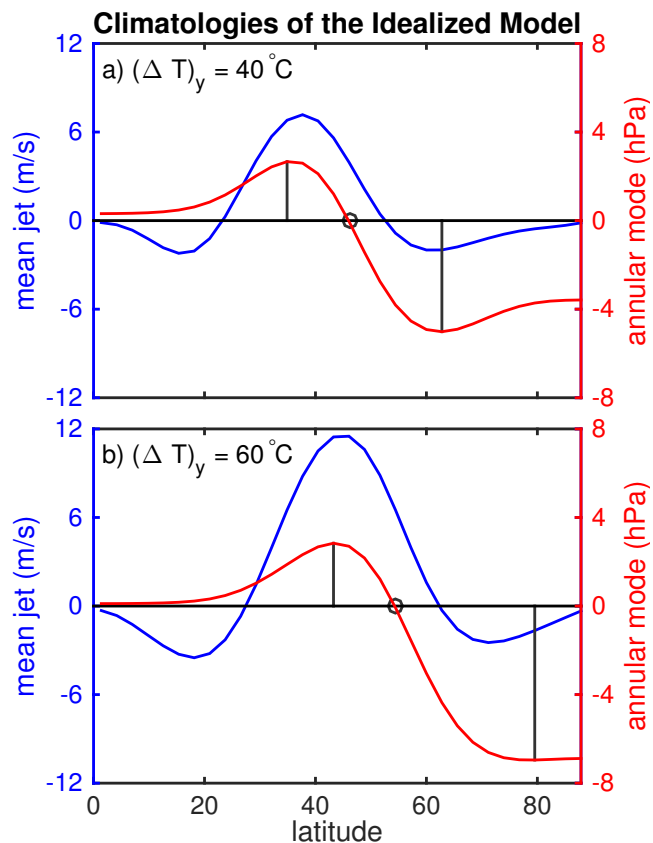


FIG. 4. The mean jet structure and annular modes of the Held and Suarez (1994) model for the (a) $(\Delta T)_y = 40$ and (b) $(\Delta T)_y = 60^\circ\text{C}$ integrations. The jet is characterized by the time mean 850 hPa winds (blue lines, corresponding with the left y-axes), and the annular mode is the first EOF of daily, zonal mean SLP (red, right y-axes), normalized to indicate the strength of 1 standard deviation anomalies. The latitudes of the node, equatorward and poleward lobes of the annular mode are highlighted, and correspond with the analysis in Fig. 5.

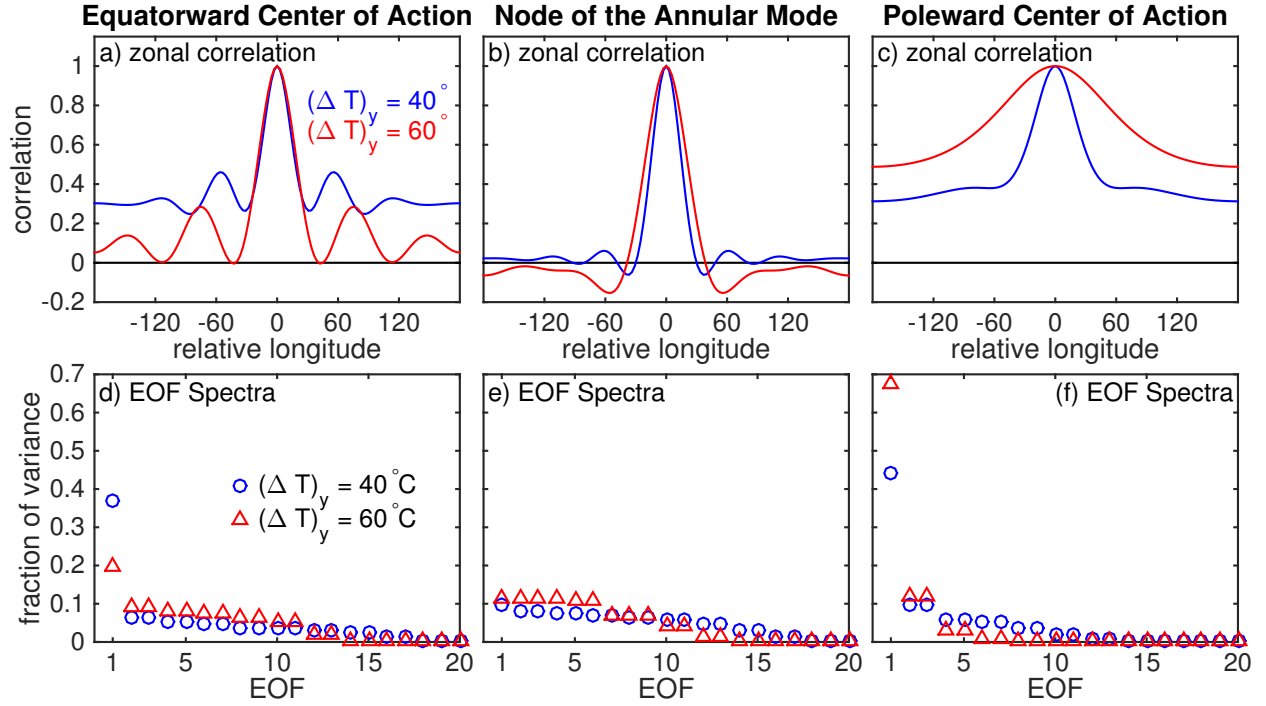


FIG. 5. Characterizing the zonal structure of 10 day pass filtered SLP anomalies in the Held and Suarez (1994) model. (a,d) and (c,f) show analysis based at the latitude of the equatorward and poleward centers of action of the annular mode, respectively, while (b,e) show analysis based at the nodes of the annular mode. (a,b,c) show the zonal correlation structure $f(\lambda)$ and (d,e,f) the fraction of variance associated with each of the top 20 EOFs for the integrations with (blue) $(\Delta T)_y = 40$ and (red) $(\Delta T)_y = 60^\circ\text{C}$.

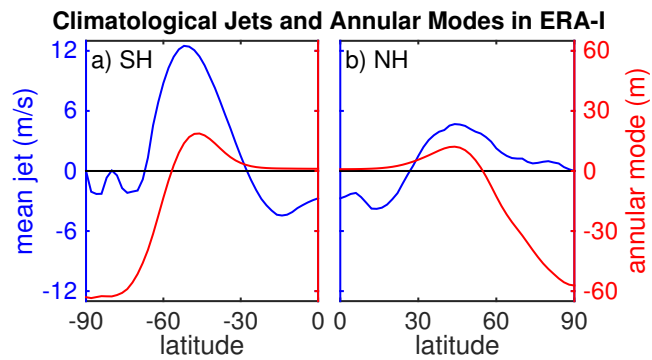


FIG. 6. The same as Fig. 4, but for the (a) Southern and (b) Northern Hemispheres in ECWMF Interim reanalysis, based on the period 1979-2013. To avoid interpolation over mountainous regions, the annular modes are defined in terms of daily, zonal mean 850 hPa geopotential height, Z_{850} , instead of SLP.

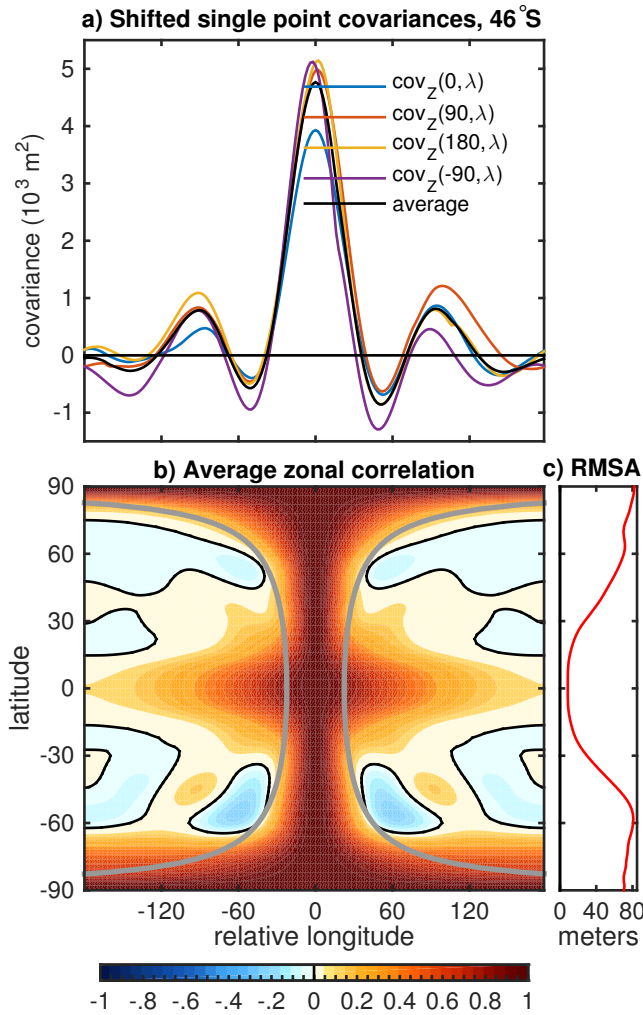


FIG. 7. Characterizing the longitudinal correlation structure of 10 day low pass filtered 850 hPa geopotential height in ERA-Interim. (a) Sample single point correlation maps at 46°S (the equatorward center of action of the SAM), shifted so that base points line up. The black line is the mean of the four curves, an “average single point correlation map”. (b) The average zonal correlation structure of 10 day low pass filtered Z_{850} as a function of latitude. The contour interval is 0.05, with black contours marking zero correlation, and gray lines indicate a separation of 5000 km, to provide a sense of geometry on the sphere. (c) The root mean square amplitude of 10 day low pass filtered Z_{850} anomalies.

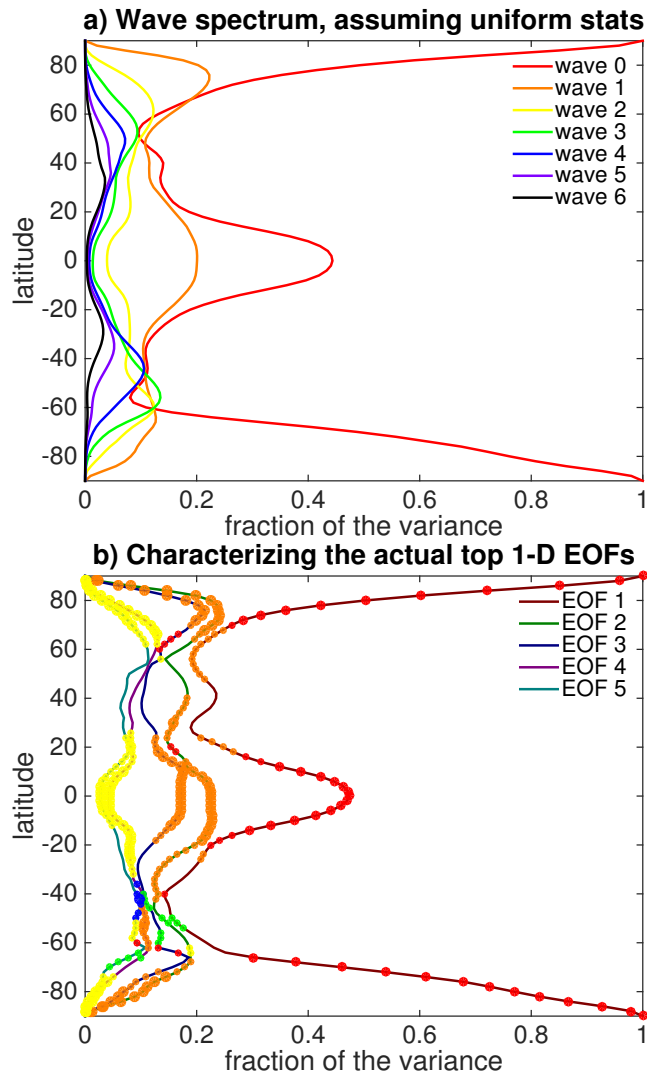


FIG. 8. A comparison of predictions based on zonally uniform statistics to the actual zonal EOF structure of 10 day low pass filtered Z_{850} . (a) For each latitude, the fraction of variance associated with wavenumbers 0 to 6, given the average zonal correlation structure in Fig. 7b and assuming zonally uniform statistics (see text for details). (b) Again for each latitude, the fraction of variance associated with the top five 1-D longitudinal EOFs, but now based on the full flow. Large (small) colored dots indicate when a given wavenumber dominates more than 75% (50%) of the power in the EOF, the color identifying the respective wavenumber with the color convention in (a), i.e., red=wave 0, orange=wave 1.

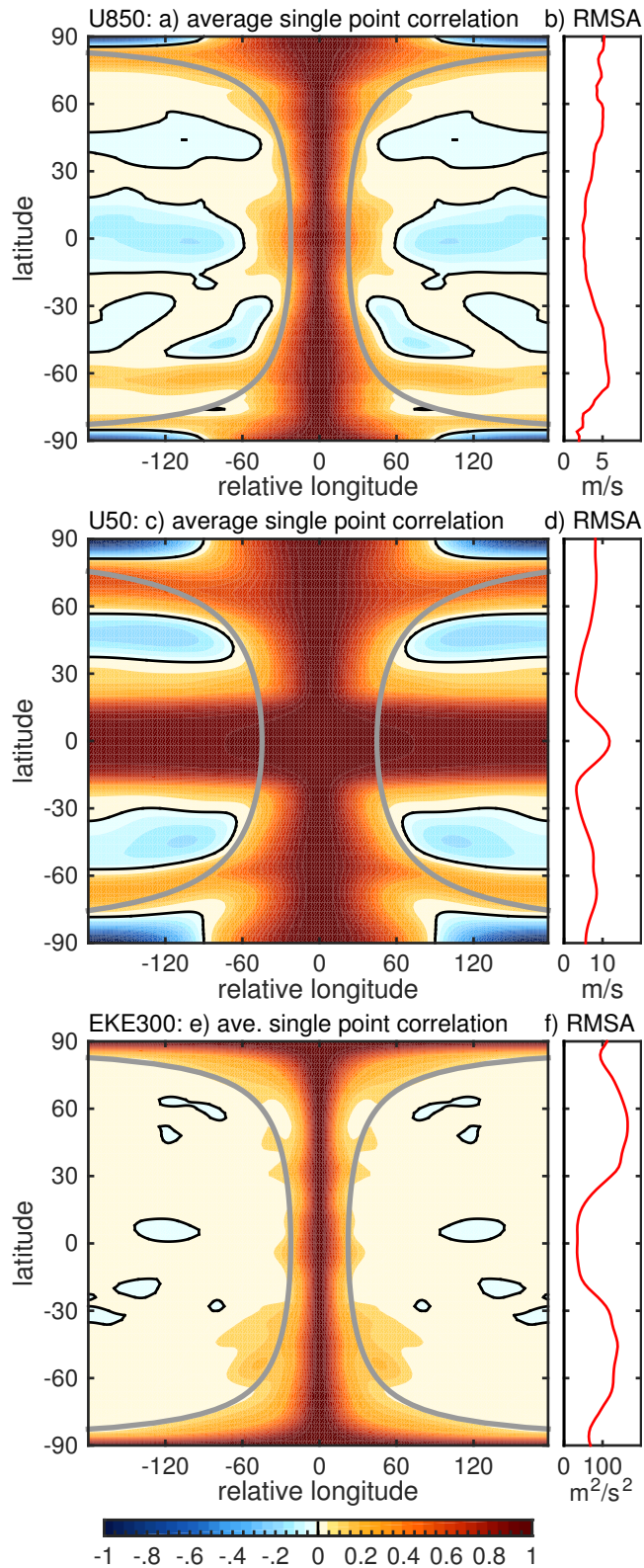


FIG. 9. The average correlation structure of (a) zonal wind at 850 hPa, (c) zonal wind at 50 hPa, and (e) eddy kinetic energy at 300 hPa. As in Fig. 7b, thin black contours mark zero correlation and the thick gray contours give a sense of sphericity, marking a separation of 5000 km as a function of latitude in (a) and (e) and a distance of 10000 km in (c). Panels (b), (d), and (f) show the root mean square amplitude of variations as a function latitude for each variable, respectively.

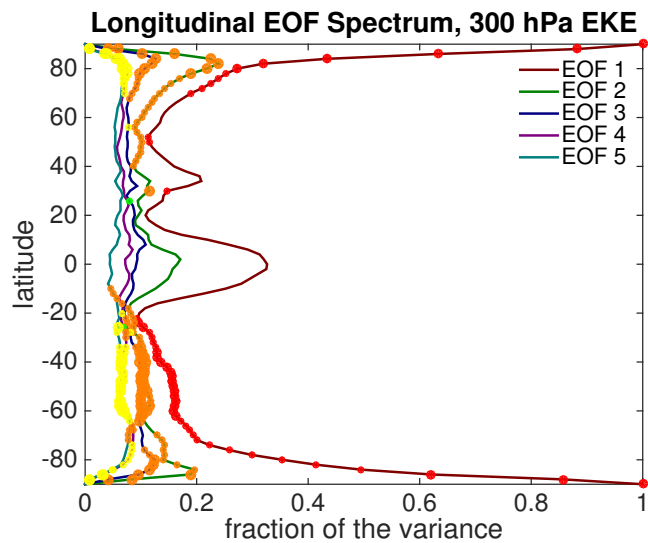


FIG. 10. The same as in Fig. 8b, but for eddy kinetic energy at 300 hPa. Zonal asymmetry in the statistics lead to substantial mixing between wavenumbers in the Northern Hemisphere (outside the polar cap) and tropics, such no single wavenumber dominates each EOF. Statistical annularity in the Southern Hemisphere, however, leads to a clearly order spectrum poleward of 25°S, dominated by an annular (wavenumber 1) mode at all latitudes.

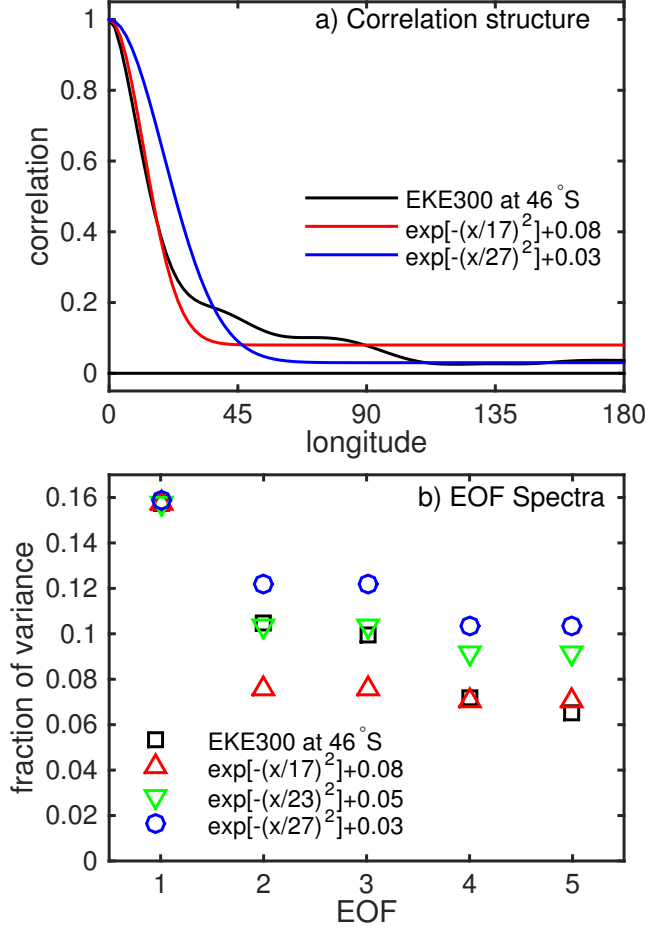


FIG. 11. (a) Comparison between the average longitudinal correlation structure of EKE_{300} at 46°S and two possible fits with the Gaussian + baseline model of Section 3. As detailed in the text, the first fit (red) is optimized to capture the initial decay in correlation, while the second fit (blue) is optimized for the long range correlation baseline. (b) The 1-dimensional EOF spectra of EKE_{300} at 46°S , compared against the spectrum for the two fits of the Gaussian + baseline model shown in (a), and a third model with parameters $\alpha = 23^\circ$ and $\beta = 0.05$, as discussed in the text.